Analysing explosive volcanic deposits from satellite-based radar backscatter, Volcán de Fuego, 2018

E. W. Dualeh[1], S. K. Ebmeier[1], T. J. Wright[1], F. Albino[2], A. Naismith[2], J. Biggs[2], P. A. Ordoñez[3], R. M. Boogher[3]and A. Roca[3]

[1]COMET, School of Earth and Environment, University of Leeds, Leeds LS2 9JT, UK
[2]COMET, School of Earth Sciences, University of Bristol, Queen's Road, Bristol BS8 1RJ, UK
[3]Instituto Nacional de Sismología, Vulcanología, Meteorología e Hidrología (INSIVUMEH), Guatemala City, Guatemala

Key Points:

- Radar backscatter observed 3 pyroclastic flows and 9 periods of lahar activity between Jan. - Oct. in Barranca Las Lajas and 40 km^2 of ash.
- Backscatter noise is reduced by up to 38% by using dense timeseries, which aids in the extraction of more subtle explosive deposits.
- Backscatter corrections and understanding of pre-eruption scattering properties are necessary for a detailed analysis of explosive deposits.

Corresponding author: Edna W. Dualeh, eeewd@leeds.ac.uk

Abstract

Satellite radar backscatter has the potential to provide useful information about the progression of volcanic eruptions when optical, ground-based, or radar phase-based measurements are limited. However, backscatter changes are complex and challenging to interpret: explosive deposits produce different signals depending on pre-existing ground cover, radar parameters and eruption characteristics. We use high temporal- and spatial-resolution backscatter imagery to examine the emplacement and alteration of pyroclastic flows, lahars, and ash from the June 2018 eruption of Volcán de Fuego, Guatemala, drawing on observatory reports and rain gauge data to ground truth our observations. We use dense timeseries of backscatter to reduce noise and extract deposit areas. Backscatter decreases where six flows were emplaced on 3 June 2018. In Barranca Las Lajas, we measured a 11.9-km-long flow that altered an area of 6.3 km^2 and used radar shadows to estimate a thickness of 10.5 $\pm$2 m in the lower sections. The 3 June eruption also changed backscatter over an area of 40 km^2, consistent with ashfall. We use transient patterns in backscatter timeseries to identify nine periods of high lahar activity in B. Las Lajas between June and October 2018. We find that the characterisation of subtle backscatter signals associated with explosive eruptions is assisted by (1) radiometric terrain calibration, (2) speckle correction, and (3) consideration of pre-existing scattering properties. Our observations demonstrate that SAR backscatter can capture both the emplacement and subsequent alteration of a range of explosive products, allowing the progression of an explosive eruption to be monitored.

1 Introduction

During an explosive volcanic eruption, monitoring can be impeded by both cloud coverage and damage to instrument networks. However, satellite-based Synthetic Aperture Radar (SAR) images are unaffected by cloud and can provide frequent observations of the progression of an eruption. While measurements from differential Interferometric Synthetic Aperture Radar (InSAR) are increasingly widely used for volcano monitoring (e.g. Fournier et al., 2010; Pritchard et al., 2018; Ebmeier et al., 2018), radar backscatter from individual SAR images (e.g. Wadge et al., 2011, 2012) has been under-exploited. Backscatter changes can be high magnitude and obvious (e.g. dome collapse, Pallister et al., 2013), or very subtle (e.g. ash dispersion, Arnold et al., 2018). The interpretation of SAR backscatter for volcanology is challenging because there is no simple relationship between the magnitude or sign of backscatter change and the physical properties of fresh volcanic deposits. Backscatter signals from explosive deposits are particularly difficult to interpret because their thickness varies over several orders of magnitude and because of their tendency to be rapidly eroded.

We use imagery spanning the 3 June 2018 eruption of Volcán de Fuego to investigate the potential of backscatter for monitoring explosive eruptions. We characterise the backscatter changes associated with pyroclastic flows, lahars, ash and investigate post-emplacement reworking by water and numerous lahars over a four month period.

1.1 Synthetic Aperture Backscatter

Radar backscatter, σ, is the proportion of the transmitted electromagnetic pulse that the ground surface directs back towards the satellite. For an area with multiple scatterers, the backscatter coefficient (σ°) is the radar cross section (σ) normalised by the area illuminated by the satellite (A) and expressed as,

$$\sigma^\circ = \frac{4\pi R^2 \rho_R}{\rho_T A} \tag{1}$$

where ρ_T and ρ_R are the power density transmitted from the satellite antenna towards the Earth and returned to the satellite sensor respectively, and R is the distance or range between sensor and target. σ° is sensitive to changes in the satellite parameters (local incidence angle, wavelength λ and polarisation) and the scattering properties of the ground. Variables including surface roughness, local slope, and dielectric properties combine to determine the

scattering properties of the ground surface. Erupted material may alter one or all of these scattering properties, which are also affected by independent non-volcanic processes such as rainfall, producing complex backscatter signals.

1.2 Monitoring Volcanic Processes using Radar Backscatter

Over the last two decades multiple studies have used SAR backscatter to observe volcanic eruptions (Table S1). These have included measurements of dome growth (e.g. Wadge et al., 2011; Pallister et al., 2013), mapping of fresh lavas (Wadge et al., 2002, 2012; Goitom et al., 2015; Arnold et al., 2017; Di Traglia et al., 2018), lava lake heights (e.g. Barrière et al., 2018; Moore et al., 2019) and flow thicknesses (Wadge et al., 2012; Arnold et al., 2017) measured using radar shadows.

Explosive volcanic deposits are more challenging to analyse in backscatter, but major pyroclastic flows have been identified both in single backscatter images (Carn, 1999) and using multi-image composites (Wadge et al., 2011). Finer and more widespread volcanic deposits such as ash produce subtle backscatter changes. Four studies have identified ash deposits (Wadge & Haynes, 1998; Goitom et al., 2015; Meyer et al., 2015; Arnold et al., 2018) and show that signals are strongly related to the pre-existing surface roughness and whether ash infills and smooths the surface on the scale of the satellite wavelength, or changes a specular reflecting surface (e.g. ice) to one that scatters diffusely (e.g. Arnold et al., 2018).

1.3 The 2018 Eruption of Volcán de Fuego, Guatemala

Volcán de Fuego (3763 m a.s.l.) is the southernmost and currently most active crater of the Fuego-Acatenango volcanic complex in Guatemala, located $\sim$ 40 km southwest of the capital, Guatemala City. Since the first written record of activity at Fuego in 1524, the volcano has had $\sim$ 60 subplinian eruptions (Global Volcanism Program, 2005) separated by long periods of intermittent Strombolian activity, making it one of the most active volcanoes in Central America. Periods of high activity at Fuego are characterised by frequent Strombolian eruptions, producing short lava flows (100s m), lahars and ash explosions (Patrick et al., 2007; Lyons et al., 2010). These periods are interspersed with high magnitude explosive eruptions, known as paroxysms (Martin & Rose, 1981). These paroxysms are short lived ($\sim$ 24 - 48h) eruptions that produce longer lava flows (100s - 1000s m), pyroclastic flows,

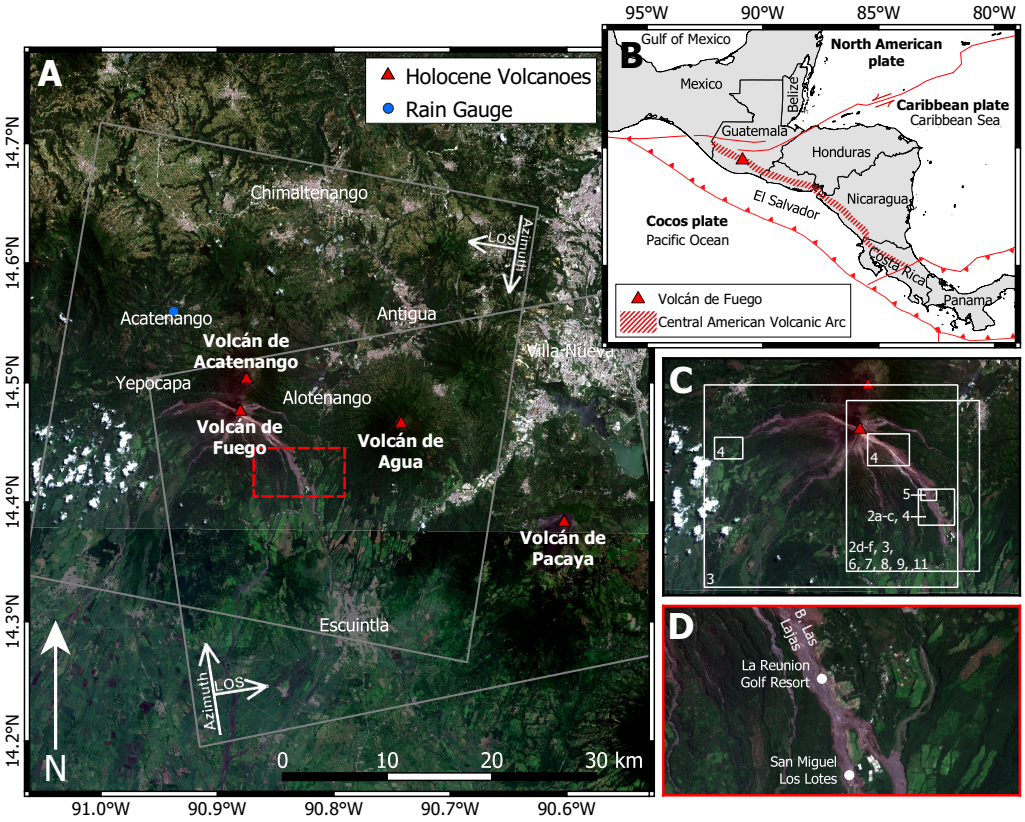

Figure 1. (a) Map of Volcán de Fuego showing the footprint of COSMO-SkyMed tracks and look direction (white rectangle), with (b) location of Fuego within Guatemala. (c) spatial extents used for subsequent figures in this article are shown by white outlines with corresponding figure number and (d) names of settlements and notable locations. (Basemap: 11 Nov. 2018 and 04 July 2018, Copernicus Sentinel-2 data)

and are able to produce and sustain an eruptive column. Volcán de Fuego is monitored by INSIVUMEH (Instituto Nacional de Sismología, Vulcanologia, Meteorologia e Hidrología), who are responsible for monitoring and communication on natural hazards, including volcanic activity to the government and private sector.

The current period of activity started in 1999 (Lyons et al., 2010) with eruptive intensity increasing in 2015 (Naismith et al., 2019). The 3 June eruption was an unusually large paroxysm (Naismith et al., 2019), with much longer pyroclastic flows and activity that increased in intensity during the eruption. The eruption began on 3 June 2018 at 06:00 local time with frequent strong summit explosions accompanied by pyroclastic flows and a plume that reached up to 17.5 km a.s.l (Pardini et al., 2019). The first pyroclastic flows

were emplaced on the western flanks of the volcano. By 14:00 local time, pyroclastic flows had descended six drainage ravines on the east and west flanks. These included multiple flows inside B. Las Lajas (Fig. 1). Most of the pyroclastic flows were restricted to the upper flanks of Fuego. However, the series of pyroclastic flows in B. Las Lajas extended over 12 km from the summit, longer than all the other flows, and buried the town of San Miguel Los Lotes (Fig. 1d), killing several hundreds of people. Official numbers report 332 people missing as a result of the eruption, although the death toll could be as high as 2,900 people (Naismith et al., 2020).

The eruption ended after 16 hours, when activity was reduced to an ash column of $\sim$ 4,500 m a.s.l (INSIVUMEH, 2018c) and weak to moderate explosions at the summit. Over the following days activity level remained high, with multiple pyroclastic flows recorded on the 5^{th}, 7^{th}, 8^{th} and 12^{th} June, dominantly on the east flank of Fuego. Interaction between the freshly deposited material and high levels of rainfall resulted in frequent lahars: INSIVUMEH reported 65 lahars between 3 June and 1 July 2018.

1.4 Backscatter Dataset

COSMO-SkyMed (CSK) is a constellation of four X-band (3.1 cm) satellites, with a 2 x 3 metres pixel dimensions in radar geometry in stripmap mode. We used 62 HH-polarised acquisitions from an ascending (H4-0B) and descending (H4-03) track between January and October 2018. This time frame includes a typical Fuego paroxym in February 2018, the unusually large 3 June 2018 paroxysm, the three months prior to the 3 June paroxysm that were uncharacteristically quiet compared to recent activity and the four months after the eruption that encompassed smaller pyroclastic flows, multiple lahars and the transition from the dry to wet season. The wet season lasts between April and September, with a pause in rainfall during July, known as the canicula. Acquisition intervals range from 1 to 8 days, with an average perpendicular baseline between images of 690 m (ranging from 6 to 1890 m).

1.4.1 Corrections and Calibrations

We produced full resolution geocoded backscatter images using the GAMMA remote sensing software (Werner et al., 2000), with all images resampled to the geometry of a common date to facilitate comparison. Slopes facing towards or away from a side-looking SAR sensor will appear in radar images to be either foreshortened or lengthened respectively.

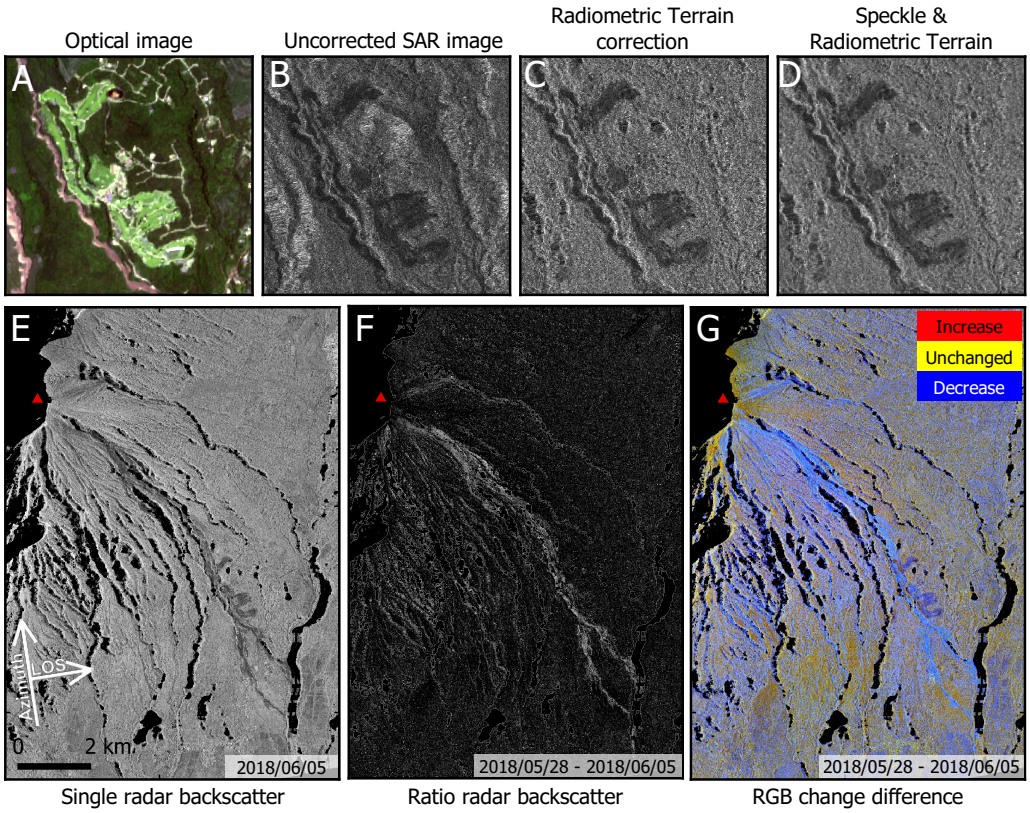

Figure 2. La Réunion golf course in (a) Sentinel-2 optical imagery (20-04-2018), (b-c) backscatter corrections and (e-g) visualisation methods applied to ascending CSK images. (b) uncorrected single backscatter image (2018-06-05) over the La Réunion golf course, (c) with a radiometric terrain correction and (d) with a radiometric terrain correction and a 5 x 5 pixel Gamma-*MAP* speckle correction. (e) single backscatter image showing the 3 June 2018 eruption, (f) ratio and (g) RGB change difference of pre- and post-eruption backscatter. Location of the scene is shown in Fig. 1c.

If the slope's gradient is steeper than the radar incidence angle, returns from the top of the slope reach the satellite before those from the bottom, producing a layover effect. Similarly, steep slopes facing away from the satellite cast a shadow, from which no information is scattered back to the SAR sensor. To mitigate the impact of topography on backscatter we make a terrain-based radiometric calibration (Fig. 2c) using 10 m resolution digital elevation models (DEMs), constructed from pairs of TanDEM-X bistatic images acquired on 18/10/2015 and 09/08/2018 (Albino et al., 2020). The radiometric terrain correction uses the DEM to increase the accuracy of the pixel area estimation used in the normalisation of the backscatter coefficient. The calibration also reduces the sensitivity to the incidence

angle by normalising the backscatter coefficient by the cosine of the incidence angle (Small, 2011; Meyer et al., 2015).

Speckle, the constructive and destructive interference from individual scatters within a pixel, causes backscatter changes even in pixels that would otherwise remain stable between acquisitions. Speckle in SAR images can obscure signals in backscatter and complicate the data interpretation. We applied a 5 x 5 pixel adaptive Gamma-*MAP* filter, which reduces speckle while attempting to preserve structural and textural features in the radar data (Lopes et al., 1993). We found that this filter preserved the sharp boundaries of the fresh pyroclastic flow deposits and man-made structures (e.g. golf course, Fig. 2d) whilst reducing the speckle allowing for better comparison between acquisitions.

2 Backscatter Analysis of the June 2018 Fuego Eruption

We describe the characteristics of the major explosive deposits from the June 2018 eruption as they appear in SAR backscatter, first using simple approaches, before establishing generalisable techniques for deposit identification and then exploring the potential for automated mapping. We use the ratio of two backscatter images (Fig. 2f) to emphasise areas that have changed (Wadge et al., 2002), and use RGB composites for visualisation (Fig. 2g, Wadge et al., 2011) where we display the later date in the red band, the earlier date in the green band and their ratio in blue. Increases in backscatter therefore appear magenta, and are mostly associated with the ground has becoming rougher due to the emplacement of the pyroclastic flow (e.g. pyroclastic flow deposits around the La Réunion golf course, lower B. Las Lajas, Fig. 2g). Decreases in radar backscatter appear cyan, and are largely associated with smoothing between acquisitions (e.g. Upper B. Las Lajas, Fig. 2g). Areas that do not change between acquisitions (e.g. 10 km southwest from Fuego's summit, Fig. 2g) appear yellow.

The major pyroclastic flow that descended B. Las Lajas during the 3 June 2018 eruption caused an overall decrease in backscatter (Fig. 3). There is a broad zone of backscatter change near the summit, which narrows as flows are funnelled into drainage channels. Here material is removed, reworked and moved downslope before being deposited, blanketing the ground surface (Albino et al., 2020). The fresh blanket reduces the backscatter (blue, Fig. 4a) by making the ground smoother on the scale of the X-band radar wavelength (i.e. CSK, 3.1 cm). However, in the middle of the pyroclastic flow path in B. Las Lajas there is a 60 m

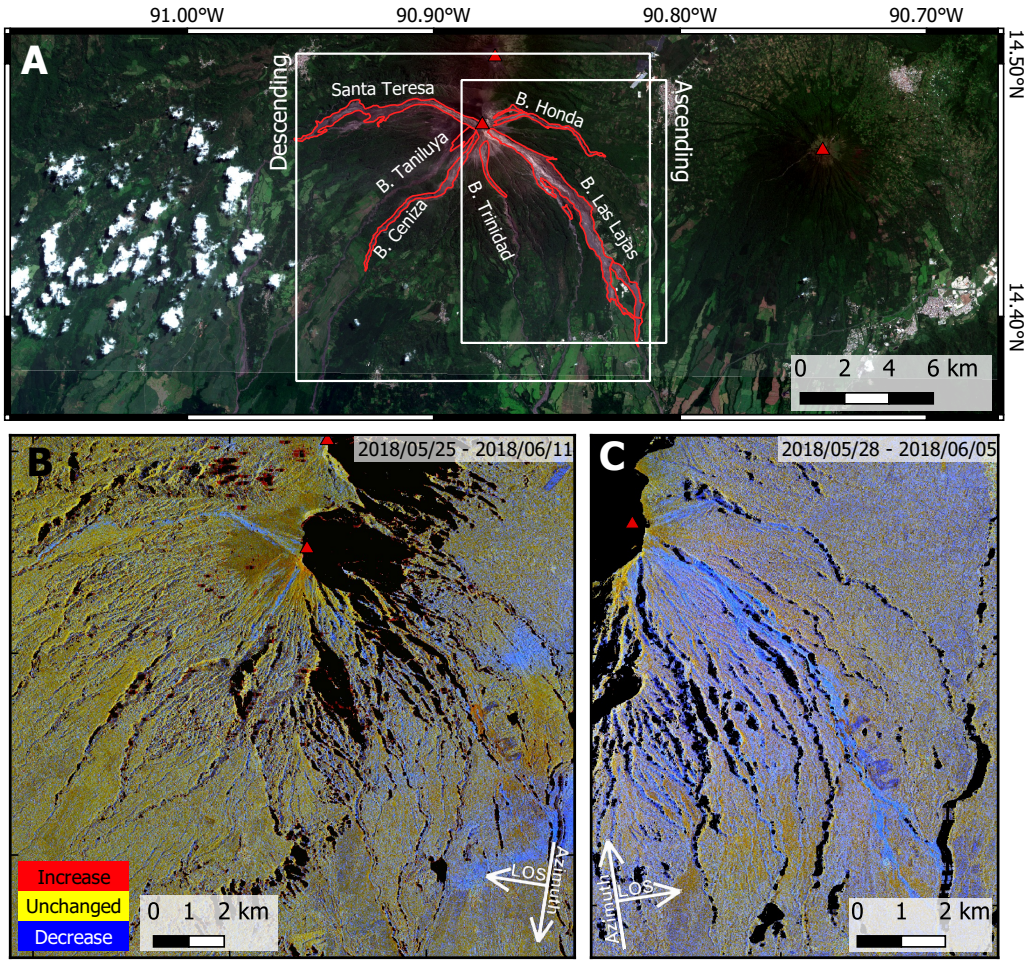

Figure 3. a) Map of the main drainage systems on Fuego affected by the 3 June 2018 eruption, as seen RGB change difference image using (b) ascending and (c) descending track showing backscatter changes in B. Honda and B. Las Lajas on the east flank and B. Santa Teresa, B. Taniluya and B. Ceniza on the west flank. Location of the scene is shown in Fig. 1c.

wide channel-like feature where backscatter increases (red, Fig. 4a). Where the pyroclastic flow has overtopped the drainage channel, the changes in backscatter depend strongly on the scattering properties of the previous surface cover resulting in complex change patterns in the lower drainage systems (e.g. dense vegetation or bare rock, Fig. 4). Where a pyroclastic flow removes vegetation the ground becomes smoother and the contribution of volumetric scattering is removed, resulting in a decrease in backscatter (e.g. forested area south of B. Santa Teresa, Fig. 4b). Backscatter change patterns differ for ascending and descending CSK tracks where the pyroclastic flow interacted with vegetation or buildings (e.g. La

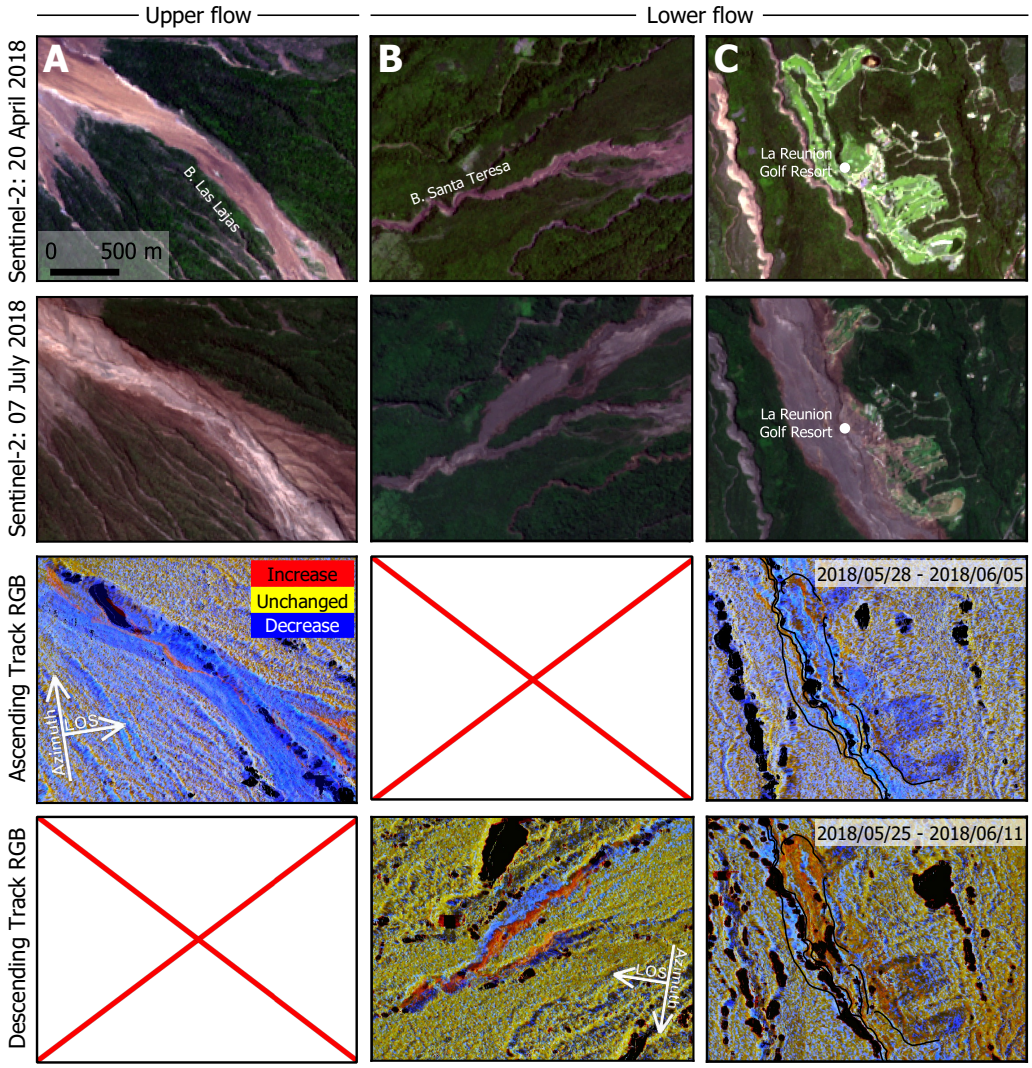

Figure 4. Backscatter changes associated with the 3 June 2018 eruption in different sections of the drainage systems. Pre- and post-eruption optical imagery and ascending CSK RGB image of (a) eastern summit area affected by pyroclastic flows in B. Las Lajas and (b) the lower section of B. Santa Teresa showing the 3 June pyroclastic flow infilling and overtopping the drainage system. Blue and red overlays indicate the increases and decreases in backscatter observed from the RGB images. (c) Pre- and post-eruptive optical imagery, descending and ascending CSK RGB images over the La Réunion golf course and B. Las Lajas showing backscatter changes correlated with different satellite look direction and incidence angle. Location of the scene is shown in Fig. 1c.

182 Réunion golf course, Fig. 4c), because scattering properties vary depending on the angle
183 from which an object is viewed.

2.1 Multiple Image Backscatter Analysis

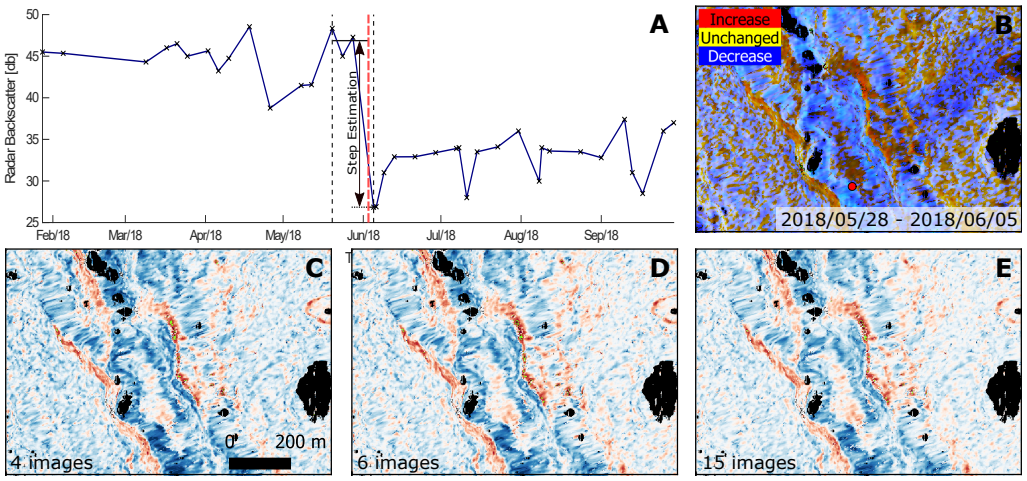

Figure 5. (a) Timeseries of single pixel (red dot in B) spanning the 3 June 2018 eruption (red dashed line) showing an acquisition time range (black dashed line) containing six images and the backscatter step calculated. The zoomed-in images over a section of 3 June 2018 pyroclastic flow in B. Las Lajas show the changes in backscatter in (b) a RGB change difference image, (c-e) a 4-, 6- and 15-image step estimation. Location of the scenes is shown in Fig. 1c.

Changes in backscatter images between two dates can be noisy, and impacted by non-volcanic effects such as changes in moisture levels. We can improve our detection of volcanic changes by exploiting our dense dataset. One simple approach is to solve for the step associated with changes in backscatter that occur on a particular date, placing no constraint on whether the step should be positive or negative. Using a pixel-by-pixel least squares inversion (Fig. 5a), we found that at least four images were required to see an improvement in the sharpness of flow edges when compared to the ratio between two backscatter images. This method allowed for better identification of flow boundaries (Fig. 5c,d), and lower magnitude changes that were not visible in RGB ratio images (Fig. 6c). The variance of backscatter change was reduced by 31% by using a total of four rather than two images, and the addition of more dates reduced the variance even further to 38% and 42% for 6 and 15 images respectively.

To refine our map of the 3 June 2018 eruption deposits, we make a step estimate using 14 backscatter images before the eruption and one after to avoid contamination by later flows, slope movements, and erosion. We also observe broad, low magnitude spatially correlated

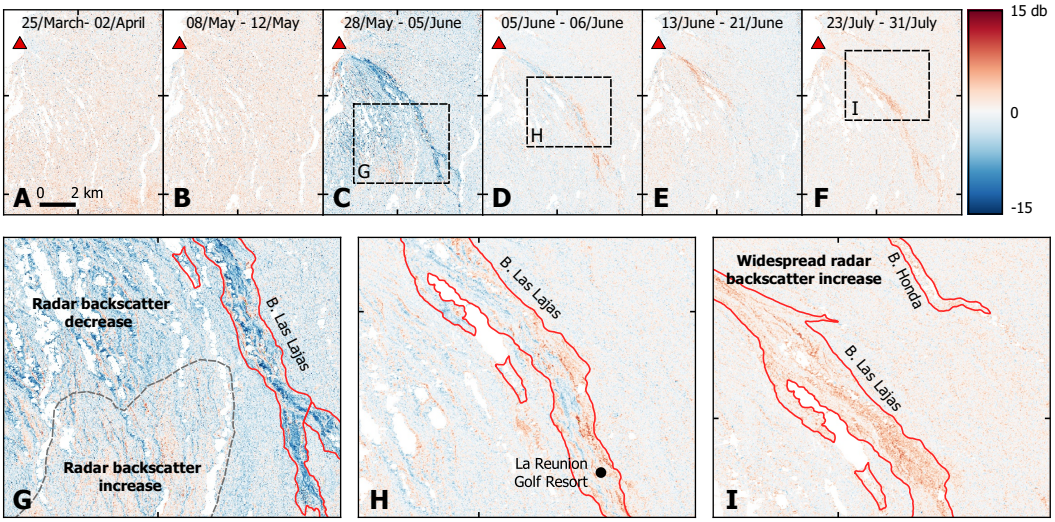

Figure 6. Step estimation (locations shown in Fig. 1c) each using four acquisition dates spanning 12 - 24 days in total showing (a-b) backscatter variations prior to 3 June 2018 eruption, (c) the emplacement of the 3 June 2018 pyroclastic flows and ash deposits and (d-f) post-eruption emplacement of new deposits, alteration and interaction with rainfall. (g-i) detailed sections of backscatter alteration seen post-eruption.

backscatter increases and decreases on the southern flank of Fuego associated with the 3 June 2018 and not apparent at any point before the eruption (Fig. 6c). The association only with the date of the main eruption, distinct spatial correlations in backscatter magnitude and sign, and limited extent are consistent with a major ash fall event rather than with changes due to rainfall. We therefore attribute it to ash emplaced on 3 June 2018 that was rapidly removed during the first rainfall event that occurred on the 5 June. Over densely vegetated areas of the flank the ash causes a decrease in backscatter whereas on agricultural land there was an increase (Fig. 6g). Reports of ash associated with the 3 June 2018 eruption suggest ash was deposited in almost every direction for about six days, with fine ash deposits extending as far as 40 km towards the northeast (INSIVUMEH, 2018b), however backscatter signals appear to be more limited.

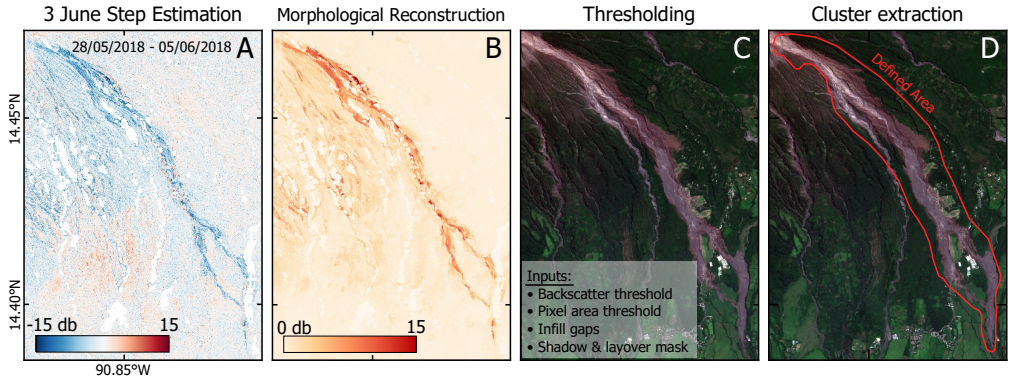

Figure 7. Semi-automatic method used to extract flow areas and lengths from (A) a four month step estimation using 15 CSK SAR acquisitions from 05 February to 05 June 2018 to extract the 3 June 2018 pyroclastic flow in B. Las Lajas. (B) Morphological Reconstruction (MR) applied to step estimation image, then using (C) multiple thresholds to clear up clusters before (D) selection of clusters associated with specific flows. Location of the scene is shown in Fig. 1c.

2.2 Identification of Explosive Deposits

2.2.1 Flow Mapping

The mapping of new flows is important to track eruption progression, update hazard assessments and protect the local communities. We can manually extract flow shapes from backscatter data, but this is both subjective and requires a longer time than may be realistic during future ongoing eruptions. We therefore test a semi-automated approach that exploits the changes in our backscatter step estimations (Fig. 7a). We consider unsupervised classification to be an appropriate approach because suitable training data is unlikely be available for a particular volcano and specific deposits type before an eruption. We use image segmentation methods aiming to keep extraction as simple as possible, and to limit the number of subjective decisions. We employ a morphological reconstruction (MR) on our step estimations prior before thresholding the image to extract large changes in backscatter associated with the emplacement of flows (Fig. 7b). MR uses a marker image based on the backscatter values to preserve object shapes whilst reducing noise (e.g. Lei et al., 2018), and we use a structuring element (10 - 20 pixels wide) in order to selectively reconstruct features with the characteristic spatial scales of flow deposits. We then apply a backscatter threshold (1.5 - 3 db for the 3rd June flows), a pixel area threshold (removing groups < 7000 m^2) and fill in any small, closed gaps within the flow using a gap size threshold

Table 1. Lengths and area measurements of Fuego drainage systems (location Fig. 1a) affected by the 3 June 2018 pyroclastic flows extracted manually and semi-automatically from the step estimation backscatter and from optical imagery (Sentinel-2, 2018/07/04). [1] measurements cited from Escobar Wolf, R. and Ferres, D. (2018).

	Honda	Las Lajas	Ceniza	Taniluya	Seca	Trinidad
SAR Flow Length (km)	6.4	11.9	8.3	1.8	9.1	> 2.5
[1]Length (km)	-	11.7	8.5	-	9.0	-
SAR area, Manual (km^2)	1.2	6.3	1.7	0.5	2.9	> 0.6
SAR areas, Semi-automatic (km^2)	0.4	4.0	0.2	-	1.1	-
SAR Percentage decrease (%)	83.3	39.7	88.2	-	62.1	-
Optical area, Manual (km^2)	1.4	7.4	1.8	1.2	3.7	1.2

(Fig. 7c). We retain larger complete gaps because they could possibly reflect real flow path structures. Lastly, we select and remove larger pixel clusters that are not associated with the emplaced flow (e.g. signals from the ash deposits) to extract the final flow shape (Fig. 7d).

We used this semi-automatic approach to estimate the areas altered by pyroclastic flows during the 3 June eruption (Table 1). Areas extracted semi-automatically from backscatter imagery were 40 - 90 % lower than those found manually (Table 1), with the biggest differences for smaller flows (e.g. B. Taniluya) where the backscatter signals are more difficult to differentiate from the surrounding noise. Estimates from the semi-automatic method are minima, because low magnitude backscatter changes, such as flow edges, overlaps with other deposits (e.g. ash) were not captured, especially near the summit or where the flows were relatively narrow. Areas estimated from optical imagery were also consistently larger than those from the SAR imagery, perhaps because very thin deposits can have a minimal impact on backscatter values for some types of land cover.

Shadows produced by the side-looking satellite radar can be used to estimate the changes in heights of the feature that cast them, (e.g. Arnold et al., 2018). However, this relies on the geometry of topographic features relative to satellite look direction, and only in the lower sections of B. Las Lajas (Fig. S1) were we able to use radar shadow to

calculate a flow thickness of 10.5 ±2 m for the freshly emplaced 3 June 2018 pyroclastic flow.

2.2.2 Exploiting Full Backscatter Timeseries

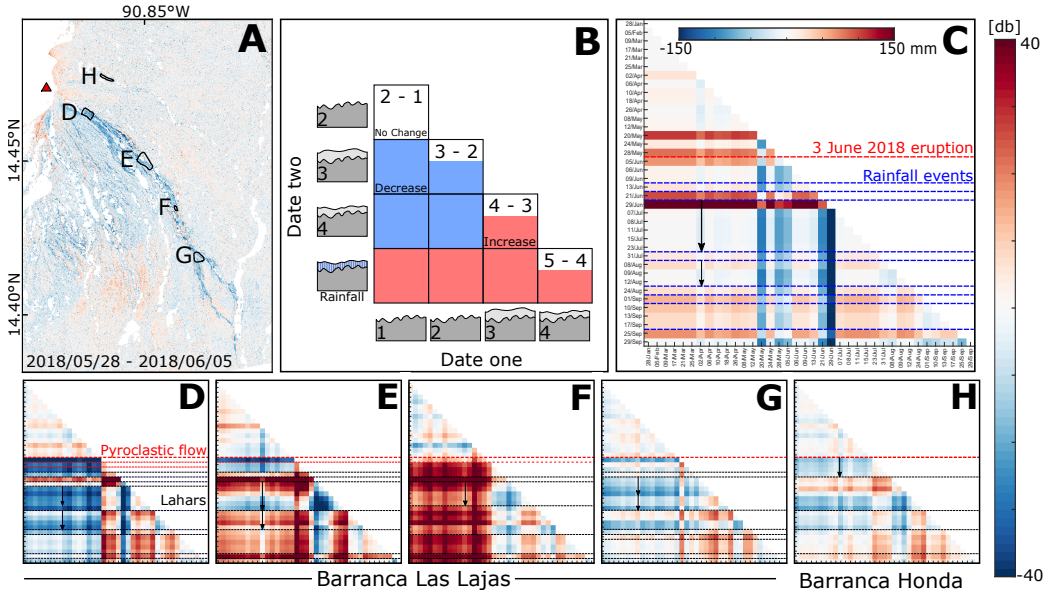

Figure 8. Backscatter change grid to show long term patterns in dataset. (A) shows the locations of each backscatter change grid (Location of the scene is shown in Fig. 1c.) (B) Schematic showing a simplified example of how a backscatter change grid is constructed. Each square represents the difference in backscatter produced from the two ground surface cartoons. The whole grid represents all possible pair combinations in the dataset. (C) Rainfall data (ICC, 2021) shown as a grid from rain gauge located 11km northwest of Fuego, location indicated on Fig. 1a. (D-H) backscatter change grids for areas along the length of B. Las Lajas and B. Honda drainage system and in overtopped deposits. Red line indicates 3 June 2018 eruption and pyroclastic flows, black line shows changes in backscatter attributed to lahar activity and blue line show changes attributed to rainfall.

Backscatter changes during an eruption may be subtle, complicated by multiple events (e.g. lahar flows) or develop slowly over an extended period of time (e.g. erosional processes). To examine these types of signals, we calculate the changes in backscatter for a particular area for all possible date combinations in our dataset (producing backscatter change grids: Fig. 8). These highlight temporal structures that allow us to distinguish between long-term

processes (e.g. erosion and material settling) and abrupt changes that correlate to specific volcanic events (e.g. lahars).

Prior to the 3 June 2018 eruption, backscatter variations were minimal for all parts of B. Las Lajas (Fig. 8d-h). The 3 June pyroclastic flows caused high magnitude changes that were strongly dependent on pre-existing scattering properties (e.g. compare the valley and the golf course in Fig. 8d and f). Backscatter changes on fresh pyroclastic deposits between pairs of images after the 3 June 2018 eruption show more complexity, and highlight structures not easily recognisable in the individual change difference images (e.g. Fig. 6). To distinguish between gradual erosion and re-working by lahars, we compare backscatter change grid patterns to rainfall data from the El Platana rain gauge (Fig. 1c, 1578 m a.s.l.; 14.56°N, 90.94°W). We found that episodes of complex changes in backscatter coincided with periods of high rainfall and matched periods of reported lahars from the INSIVUMEH bulletins.

The lack of rainfall during July at Fuego (Fig. 8c) allowed material to settle and resulted in gradual decrease in backscatter (29 June and 23 July, arrows in Fig. 8d-g). The next major rainfall after these drying periods are marked both by abrupt changes in backscatter in the drainage channels and by scene-wide increases in backscatter (Fig. 6f, i) with higher magnitudes in both the newly deposited volcanic material and the agricultural land towards the south and southeast of Fuego. When the subsurface goes from dry to wet, radar penetration into the ground decreases and there is less interaction with deeper scatterers, increasing the influence of the near-surface scatterers and returning more radiation towards the satellite. We speculate that backscatter change is higher magnitude over the looser fresh volcanic material and agricultural fields because these hold moisture better than the surrounding vegetation.

2.3 Phase Coherence of Flow Deposits

Interferometric phase coherence is very sensitive to changes in surface properties due to volcanic deposits (e.g. Wadge et al., 2002; Dietterich et al., 2012). A pixel's phase comprises contributions from all the individual scatterers within it, and its phase coherence can be estimated from the correlation between phases for a group of pixels. Exposed bed rock, roads, or any stable structure will result in high coherence values, whereas features that change between acquisitions, such as vegetation or rockfall, will cause low coherence. Both

the time span between acquisitions and satellite perpendicular baseline may be proportional to the degree of phase decorrelation.

We estimate coherence by assessing the correlation of 3x3 grids of pixels for selected areas along the 3 June 2018 pyroclastic flow in B. Las Lajas using all possible image pairs within our dataset. The large perpendicular baseline range of CSK images, average of 690 m between acquisitions, results in very high geometric decorrelation and many images that are entirely incoherent. By plotting the perpendicular baseline against the average coherence we identify a perpendicular baseline threshold of >700 m at Fuego, beyond which we lose coherence except where the temporal baseline is especially low (e.g. one day interferograms).

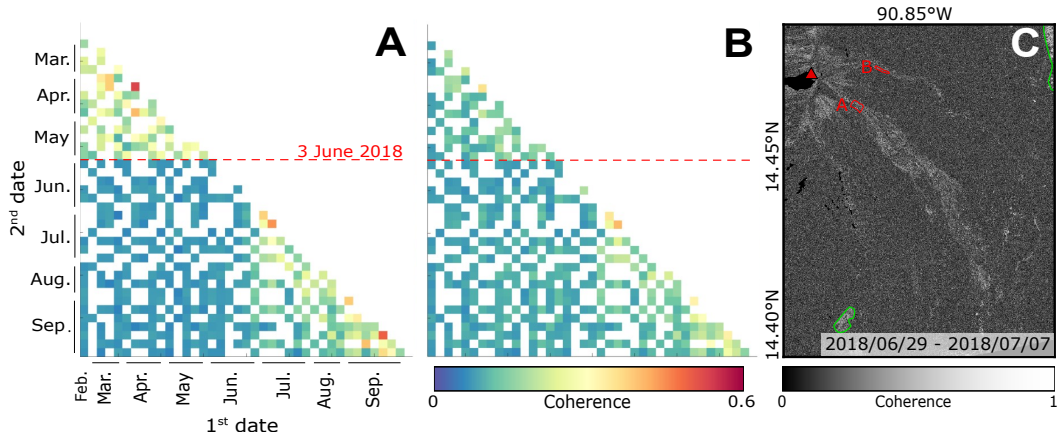

Figure 9. Radar coherence matrix for the upper sections in (a) B. Las Lajas and (b) Honda for areas shown in red in (c) coherence image (D and H, Fig. 8a) showing the complete loss of coherence associated with the 3 June 2018 pyroclastic flow, the short-term reappearance at the end of June and the return to pre-eruption coherence levels by September 2018. Coherence matrix represent the same temporal scale with white squares representing perpendicular baselines >700 m. High coherence that correlates to towns and agricultural fields outlined in green.

Coherence over Fuego is very low with only $\sim 7\%$ of the 100 km^2 around B. Las Lajas and Honda showing a coherence over 0.5, even for perpendicular baseline <700 m. High coherence is limited to towns and some agricultural fields (Fig. 9c), while dense vegetation and steep slopes lead to low coherence on the volcano. Prior to the June eruption, the drainage systems on the volcano flanks showed higher coherence but the emplacement of the pyroclastic flow on 3 June 2018 resulted in a sudden loss of coherence (Fig. 9). In B. Las Lajas, the complete loss of coherence lasted for approximately a month before higher

coherence values reappear. These higher coherence values in July 2018 correspond to the break in the rainy season and temporary pause in lahar activity (Fig. 10a). Post-July the coherence drops slightly as the increased number of lahars slowly reworked the material in B. Las Lajas. The scattering properties gradually stabilise during September 2018 and return to the pre-eruption coherence levels. Similar trends are visible in B. Honda (Fig. 9b) demonstrating the strong correlation between lahar activity, rainfall and coherence levels.

3 Discussion

3.1 3 June 2018 Explosive Deposits

Six drainage systems at Fuego showed changes in backscatter as the result of pyroclastic flows on 3 June 2018 (Fig. 3), as described in the INSIVUMEH special bulletins (INSIVUMEH, 2018c). These newly emplaced pyroclastic flows follow the pre-existing drainage down the flanks of the volcano (Fig. 3). Our measurements show that the multiple flows in B. Las Lajas extend up to 11.9 km from the summit, altering a total area of 6.3 km^2 (Table 1) with flow thicknesses of up to 10.5 $\pm$2 m in the lower sections of the drainage where the flow accumulated against the valley edge. Our thickness estimate compares well with topographic increases of 12 m derived from TanDEM-X data (Albino et al., 2020) for the lower portions of B. Las Lajas. Overall, flow lengths we measured from the backscatter (Table 1) were within 0.2 km of ground-based measurements (Escobar Wolf, R. and Ferres, D., 2018). Near the summit the flows funnelled into different drainage systems reduced the surface roughness. The narrow band of backscatter increase we observe in B. Las Lajas 4b) is likely to be caused by local increases in cm-scale roughness associated with a central higher energy flow, transporting a wider range of material than in the surrounding channel. These localised increases in backscatter correlate roughly with the collapse and transitional facies described in Albino et al. (2020), where material was dominantly removed. Although changes in local slope caused by the incision of a small higher energy inner channel, could also cause bands of backscatter increase, there is no indication of a new channel in the post-eruption backscatter image (05/06/2018). Further down the drainage system, deposits were generally bounded by the channel wall and the backscatter changes are associated with different stages of valley infill and in some areas overtopping (Fig. 4b).

An approximately 40 km^2 wide area on the southern flank of Fuego showed subtle changes in backscatter that we attribute to ashfall from the initial 3 June 2018 eruption (Fig.

6c, g). These changes are apparent only in the co-eruptive step estimation images (Section 2.1), which reduced the background backscatter noise. The origin of this change is unclear, but we attribute the backscatter decrease to the emplacement of a layer of ash, rather than the removal of leaves from vegetation, since this would produce long-term changes in backscatter that we do not observe. The impact of this ash layer on the backscatter images was short-lived and completely disappears from all other post-eruption images, which were acquired after the first major post-eruption rainfall.

Following the 3 June 2018 eruption, the backscatter remained low within B. Las Lajas (Fig. 6d, h, 8d, e). This low backscatter was concentrated to the upper slopes of B. Las Lajas, extending downslope within a defined channel (Fig. 6h) within the 3 June flow deposits. This backscatter pattern coincides with two smaller pyroclastic flows observed by INSIVUMEH on the 5 June 2018 (INSIVUMEH, 2018a, 2018d).

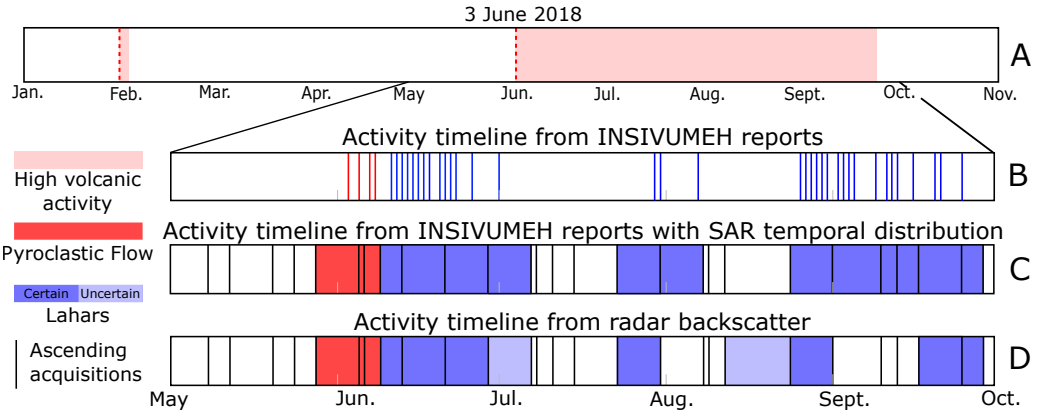

Figure 10. Timelines showing activity the various activity in B. Las Lajas. (a) shows the periods of volcanic activity in 2018 at Fuego, (b) the daily processes in B. Las Lajas as reported by INSIVUMEH, (c) the activity reported from the INSIVUMEH bulletins from the shown in the same time steps as the SAR acquisition, and (d) the timeline of volcanic activity derived from backscatter.

During June and then between August to September, Fuego had periods of high lahar activity (Fig. 10), which appeared as both increases and decreases in our backscatter change grid depending on the conditions and location of the lahar. We used the INSIVUMEH reports to ground truth our identification of lahar activity, and found good agreement between backscatter and field observations. From June to September 2018, we identified nine

possible periods of lahar activity in B. Las Lajas from backscatter alone, two of which produced small, spatially discontinuous changes or do not correlate with a major rainfall event. A period that we flagged as lahar activity with high uncertainty in June and July in B. Las Lajas was confirmed by in-situ observations recorded in INSIVUMEH reports (e.g. INSIVUMEH, 2018e). However, there were three periods with lahars reported by INSIVUMEH in September that are not clear from our backscatter analysis. This could be because flows were narrower or shorter, or missed by our choice of areas selected for our backscatter change grid. It is also possible that their erosional and depositional impact on the backscatter was minimal. Further, we potentially observed a period of lahar activity in B. Las Lajas between 12-24 August 2018 (Fig. 10) that was not reported by INSIVUMEH, but showed spatially correlated changes in backscatter throughout B. Las Lajas.

3.2 Identification of Volcanic Products from Backscatter

Here we discuss the approaches that were most successful for studying explosive eruption deposits at Fuego, including the potential for automatic extraction of flow shapes.

3.2.1 Mitigating Sources of Noise

Backscatter changes caused by explosive volcanic products may be low magnitude, small in spatial extent and differ according to scattering properties of the pre-existing land cover and topography. Interpreting backscatter therefore requires some knowledge of both pre-event scattering properties (e.g. inferred from radar, optical or ground-based imagery) and pre-existing topography (from a global, or preferably local, DEM). Maximising signal to noise ratio is also critical, and can be achieved by mitigation of noise in the backscatter.

Applying a radiometric terrain correction to the Fuego dataset reduced distortions from the steep topography allowing us to make backscatter change measurements on the steeper slopes near Fuego's summit. The high-resolution TanDEM-X-derived DEMs (10 m, 18/10/2015 and 09/08/2018) were better able to correct distortions than SRTM (30 m, 11/02/2000) (Fig. S2). Using both a pre- and post-eruption DEM for our analysis also minimised errors associated with differences between topography at the time of each SAR image and the DEM used for correction (especially the local gradient and location of drainage channels) (Fig. S3). Even with a radiometric terrain correction, major differences in the satellite geometry still affect the backscatter change if the scattering mechanisms

vary with incidence angle. For example, trees produce very different scattering signals depending on whether radar encounters the crown or the trunk first. This effect may account for the differences in backscatter change pattern that we observe between different tracks with different incidence angles in some locations (Fig. 4c). Without the application of an adaptive filter, speckle can mask shapes and structures of the explosive volcanic deposits (Fig. 2d). The adaptive Gamma-*MAP* filter (Lopes et al., 1993) improved our analysis of the backscatter changes for all methods. In our step estimation images the speckle filter made the transition between flow and surrounding areas sharper, reducing the background variance by 7% and making the subtle changes in backscatter, such as ash (Fig. 6c, g), more easily distinguishable. For major changes such as those caused by the eruptions on 3 June, the single backscatter and change difference RGB images are sufficient to identify the main deposits. However, solving for a step in backscatter using longer timeseries (>30 days) and more images improved both our mapping of flow boundaries, and allowed identification of more subtle changes in backscatter (e.g. ash fall).

3.2.2 Identification of Explosive Deposits in Backscatter

In general, the significant changes to backscatter due to pyroclastic flows are limited to drainage channels and surroundings, with the sign of backscatter change dependent on radar wavelength, flow roughness and pre-eruption scattering properties. It may take the backscatter a few days, months, or years to return to pre-eruption levels of backscatter (e.g. for vegetation to grow back where it was completely removed). However, backscatter can also remain permanently altered and never return to the values it had before the eruption (e.g. complete restructure of drainages systems).

Backscatter signatures of major pyroclastic flows have been identified at Soufrière Hills Volcano, Montserrat using TerraSAR-X (X-band) (Wadge et al., 2011) and the 2010 Merapi eruption with ALOS-PALSAR (L-band) (Solikhin et al., 2015). For Fuego (Fig. 4) and Soufrière Hills Volcano, decreases in backscatter were associated with pyroclastic surge deposits blanketing and overtopping drainage channels. However, pyroclastic surge deposits at Merapi caused an increase in the backscatter, perhaps because at Merapi darker forest was removed and covered by high energy, bright surge deposits. There are also similarities in backscatter patterns within flows at different eruptions. At Fuego and Soufrière Hills Volcano, narrow bands of increased backscatter occur in the middle of surge deposits (e.g. Fig 4a), which we attribute to fresh block and ash deposits, including larger, up to metre-

scale blocks that dominate the backscatter signal. However, the 2010 Merapi eruption, a narrow band of decreased backscatter was observed in the centre of the flow where the most energetic flows were deposited. The differences between observations at Merapi, Fuego and Montserrat are consistent with the different roughness lengths scales to which L-band (λ = 23 cm) and X-band (λ = 3.1 cm) radar are sensitive. The Rayleigh Criterion, h > $\frac{\lambda}{8cos(\theta)}$, provides a material size threshold of whether a surface is appears 'rough' (bright) or 'smooth' (dark) in backscatter. For X-band, objects <0.4 cm appear smooth while for L-band objects <3.6 cm will appear smooth. This means that material between 0.4 – 3.6 cm will produce different backscatter signals at L- and X-band wavelengths.

Lahars produce much more subtle signals in backscatter limited to active drainages and freshly deposited material. Distinguishing between the sudden changes caused by a lahar and more gradual erosion is particularly challenging using non-continuous imagery. The addition of rainfall data provides some constraint on when lahars are more likely to have occurred. The use of dense SAR timeseries with short revisit times is also critical. The Fuego lahars produce both increases and decreases in backscatter at different positions within the flow. In general, the upper sections of drainages are dominated by erosion, reducing the backscatter, while surface roughness increases downslope as larger blocks are deposited. Multiple lahars of different sizes and magnitude may occur during the several days between SAR acquisitions so that the backscatter change patterns do not represent a single change to the ground but are due to multiple events. The backscatter change caused by a lahars is also sensitive to the timing of rainfall; high rainfall closer to the second acquisition produces a higher magnitude change than if it were close to first acquisition and the ground had time to dry out. Although backscatter signals from lahars are superficially similar to those from gradual erosion and deposition in any image pair, we found that we could identify lahar signals at Fuego by finding turning points in backscatter sign in the timeseries (Fig. 8) and comparing their timing to high rainfall events (Fig. 8c).

The backscatter changes associated with the emplacement of ash from 3 June eruption are much more widespread than either the pyroclastic flows or lahars. In general, backscatter signals from ash reach their maximum close to the eruptive vent of the volcano and are characterised by short-lived changes. The sign of the change is dependent on the pre-eruption land cover, the moisture content of the ground and the ash, whether the deposit coats the ground or is thick enough to remove or destroy vegetation. Although ash deposits are spatially systematic, they may produce only very small magnitude variations in backscatter,

difficult to differentiate from background noise. Therefore, reliable corrections for noise (e.g. speckle) are necessary, especially as the impact of ash on SAR backscatter (e.g. the impact of thickness variations, morphology, dielectric properties, etc) is poorly understood. At Fuego we measure both an increase and decrease in backscatter caused by ashfall over different surfaces, but at Nabro (June 2011, Goitom et al., 2015) the pre-eruption land cover was a uniform semi-arid environment, resulting in a decrease in backscatter signal linked to topographic smoothing. For both Fuego and Nabro eruptions, backscatter changes related to ash were dominated by changes in the surface roughness. However, the ash at Cotapaxi, Ecuador (August 2015, Arnold et al., 2018) had a high moisture content producing an increase in backscatter and masking any decrease in surface roughness. Although ash can be easily observed at some eruptions (e.g. Nabro, Eritrea, Goitom et al., 2015), depending on the magnitude and ground coverage at the time it can produce a much more subtle change in the backscatter such as seen for the 2018 Fuego eruption. In these cases, longer timeseries are more adept at extracting these types of signals.

3.2.3 Potential for Automated Flow Shape Extraction

While our study of the 2018 Fuego eruption is retrospective, analysis of backscatter has great potential as a tool to track the progression of an eruption, especially where visual observations are limited. We assess the accuracy of the areas and lengths generated by our semi-automatic approach (section 2.2.1) by comparing them to measurements extracted manually from backscatter (Table 1) and optical imagery (i.e. Sentinel-2, 2018/07/04, Table 1). For B. Las Lajas the semi-automatically identified area was ∼38% smaller than through manual extraction, while smaller flows where backscatter variations were not significantly different to the background noise (e.g. B. Taniluya) showed up to ∼85% difference. Using smaller MR structuring elements and lower thresholds allowed us to extract some of these flow shapes, reducing these values too far resulted in false positives especially in areas where the surrounding variations were large (e.g. summit or ash on south flank). False positives were also associated with overlapping deposit distributions, signals from volcanic ash on the southern flank merged with changes associated to the flow in B. Trinidad and upper sections of B. Las Lajas in June 2018 (Fig. 6c).Our use of a morphological operators and image segmentation limited bias in the identification of flows. However, the semi-automatic method was less effective where backscatter changes were low magnitude (e.g. B. Honda, Fig.

3c), where changes were similar to the level of background noise, or where the boundaries showed gradual transitions (false negatives).

The flow areas measured from optical imagery (Table 1) were larger for all drainages than seen in the backscatter images. This may be because the first SAR image that was acquired two days post eruption, while the first completely cloud free Sentinel-2 optical image was acquired over a month later on the 4 July 2018 and captures multiple events, not seen in the SAR image pair. Further, some deposits (e.g. overtopped deposits in lower B. Seca, Fig. 4b) visible in the optical imagery either do not change the radar scatterers enough to cause a difference in backscatter (e.g. very thin layers), or different signal contributions (e.g. from roughness and moisture) cancel each other out. For example, the backscatter would show a decrease for a rough surface becoming smoother and an increase for a dry surface becoming wet. A rough, dry surface that changes to a smooth wet one may produce minimal backscatter change. A deposit that produces changes in all contributing factors: local slope, centimetre-scale roughness, and moisture, produces a very complicated change pattern, with the potential for some flow sections to produce minimal or non-observable change signals.

3.3 Application to Explosive Volcanoes Globally

The high spatial resolution and temporal density provided by CSK SAR images are ideal for analysis of explosive volcanic eruptions using backscatter. However, CSK is a commercial constellation and although it has a good volcano background mission, it is not free or open, although it is available to observatory and research scientists through programmes such as the CEOS Volcano Demonstrator. We therefore also examine the applicability of the methods we developed here by applying them to freely available C-band (5.6 cm) data from the Sentinel-1 (S1) satellite constellation, which provides global open access imagery with a resolution of 4 x 20 m.

The major 3 June 2018 eruption at Fuego produced fundamentally similar signals in both CSK and S1 data, which both captured changes in all affected drainage systems (Fig. 11). The pyroclastic flows in B. Trinidad (not reported in the INSIVUMEH eruption reports), which was partially masked in the CSK images due to the incidence angle, is clearer in the S1 imagery. The S1 change difference and step images showed overall similar shapes and temporal trends for the pyroclastic flows deposits, although the lower resolution does

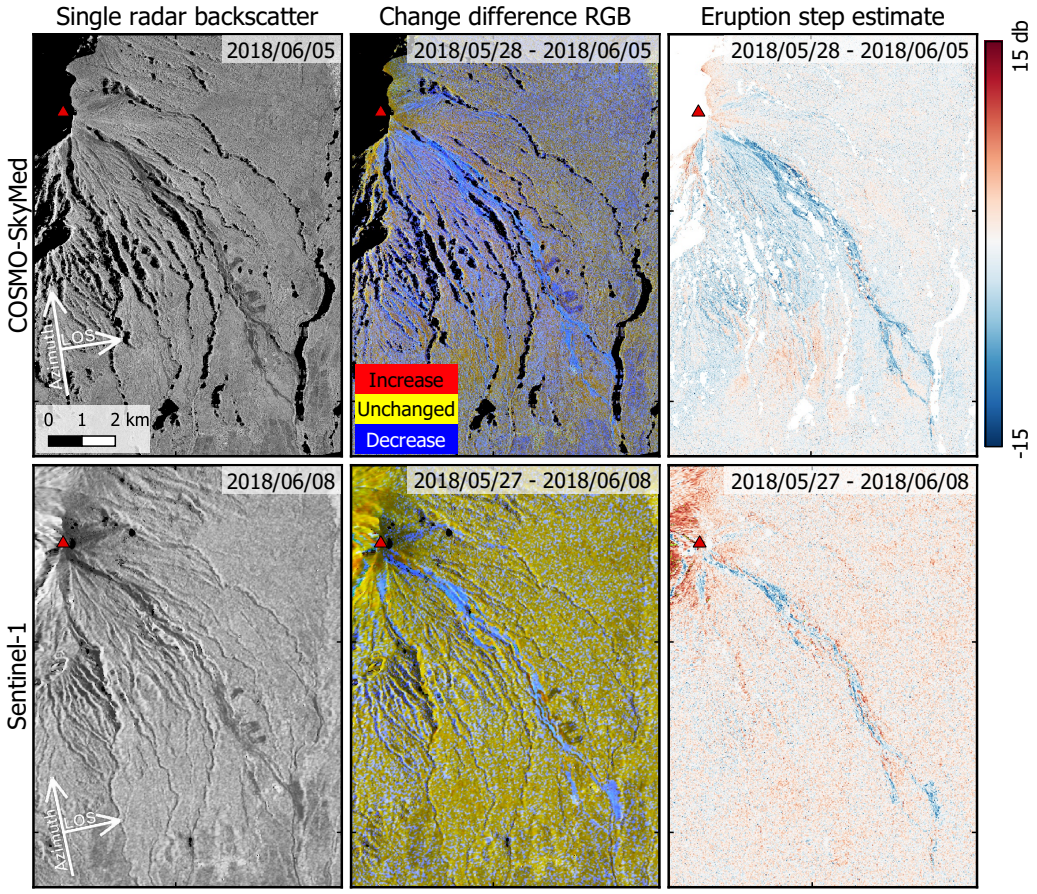

Figure 11. Comparison of S1 and CSK backscatter methods for the 3 June 2018 pyroclastic flow in B. Las Lajas. A radiometric terrain correction and speckle filters were applied to both S1 (using the SRTM 30 m DEM and a 3 x 3 pixel window) and CSK (using the TanDEM-X derived 10 m DEMs and a 5 x 5 pixel window). Location of the scene is shown in Fig. 1c

not capture the finer detail seen in the CSK data, (e.g. complexity around La Réunion golf course and the overtopping at San Miguel Los Lotes). The longer repeat time for the S1 data also results in the aliasing of more events in the step estimates, and thus masks or reduces changes associated with transient processes. Nevertheless, the global availability of Sentinel-1 data allows for frequent (6-12 day) observation and interpretation of explosive volcanic eruptions.

The initial removal of dense forest and vegetation around Fuego by 3 June 2018 eruption (Albino et al., 2020) meant that the eruption changed the surface scatters considerably when it was removed, after which changes were more subtle. Although tropical vegetation produced very low interferometric phase coherence at Fuego, in other settings (e.g. Dietterich et al., 2012), phase coherence would provide an independent comparison to flow extent maps derived from backscatter. The 3 June eruption, occurred following a few months of low volcanic activity, allowing us to build up a good baseline of backscatter variations due to moisture changes and other sources of noise before the eruption. When the eruption occurred, this allowed us to distinguish the change in backscatter associated the emplacement of fresh material.

Backscatter is most useful to examine explosive volcanic eruption in areas where there is substantial change the ground surface, for example where deposits are extensive and the volcanoes topography is significantly altered. Eruptions where ash and pyroclastic flows cover or remove dense vegetation will also produce strong backscatter changes. Similarly, eruptions that occur after long non active periods will more likely show large magnitude backscatter changes than a volcano that is continuously erupting.

4 Conclusion

We provide a thorough application of multiple backscatter methods to examine explosive volcanic deposits of the 2018 activity of Volcán de Fuego, Guatemala. We use SAR backscatter to map six drainages affected by pyroclastic flows (Table. 1) during the 3 June 2018 eruption accompanied by backscatter changes associated with ashfall. The major flow in B. Las Lajas showed an extent of 11.9 km from the summit covering an area of 6.3 km^2 and with a thickness up to 10.5 $\pm$2 m in the lower section, where we could use radar shadows to observe valley infilling. The backscatter signals associated with the B. Las Lajas deposits showed increases related to the block and ash deposits within the channel and wider spread

decreases in backscatter linked to the flow surge. Between June and September 2018, we observed two more pyroclastic flows in B. Las Lajas and, with additional information from local rainfall data and INSIVUMEH reports, nine periods of potential high lahar activity.

We demonstrate that solving for a step change in backscatter from a timeseries improved signal to noise ratio and aided the identification of explosive volcanic deposits. Our use of timeseries of backscatter change show temporal patterns that have potential to differentiate between lahars and more gradual post-eruption erosion processes.

This work demonstrates the suitability of SAR backscatter for monitoring the progression of explosive eruptions and the subsequent alteration of their deposits. We demonstrate the extraction of quantitative information from backscatter in the presence of noise, as well as the identification of pyroclastic flows, lahars and ash. This case study shows the potential of the backscatter datasets to provide useful observations and measurements for volcano monitoring when optical, radar phase or ground-based observations are limited.

Acknowledgments

This work was supported by the European Space Agency (ESA Living Planet Fellowship to SKE), the NERC-BGS Centre for Observation and Modelling of Earthquakes, Volcanoes, and Tectonics (COMET) and the University of Leeds. SKE is supported by a NERC Independent Research Fellowship. We acknowledge the CEOS Working Group on Disasters Volcano Demonstrator and ASI for providing 19 COSMO-SkyMed spanning January - October 2018. We thank Juliet Biggs, Matthew Watson, ASI and INSIVUMEH for coordinating the provision of 43 COSMO-SkyMed images spanning the June 2018 eruption (March - August 2018). CSK imagery, provided by ASI, can be requested through the CEOS Volcano Demonstrator Program, by contacting either the demonstrator leads or the WGDisasters secretariat (https://ceos.org/ourwork/workinggroups/disasters/). Sentinel-1 imagery are freely available from ESA's Copernicus Open Access Hub and older imagery can be requested from the Long Term Archives (https://scihub.copernicus.eu/userguide/LongTermArchive). We would like to thank M. Watson and H. Wright for valuable discussion on the 2018 Fuego eruption.

References

Albino, F., Biggs, J., Escobar-Wolf, R., Naismith, A., Watson, M., Phillips, J., & Marroquin,

G. C. (2020). Using TanDEM-X to measure pyroclastic flow source location, thickness and volume: Application to the 3rd June 2018 eruption of Fuego volcano, Guatemala. *Journal of Volcanology and Geothermal Research*, 107063.

Arnold, D. W., Biggs, J., Anderson, K., Vallejo Vargas, S., Wadge, G., Ebmeier, S. K., ... Mothes, P. (2017). Decaying Lava Extrusion Rate at El Reventador Volcano, Ecuador, Measured Using High-Resolution Satellite Radar. *Journal of Geophysical Research: Solid Earth*, *122*(12), 9966-9988. doi: 10.1002/2017JB014580

Arnold, D. W., Biggs, J., Wadge, G., & Mothes, P. (2018). Using satellite radar amplitude imaging for monitoring syn-eruptive changes in surface morphology at an ice-capped stratovolcano. *Remote Sensing of Environment*, *209*, 480-488. doi: 10.1016/j.rse.2018.02.040

Barrière, J., d'Oreye, N., Oth, A., Geirsson, H., Mashagiro, N., Johnson, J. B., ... Kervyn, F. (2018). Single-Station Seismo-Acoustic Monitoring of Nyiragongo's Lava Lake Activity (DR Congo). *Frontiers in Earth Science*, *6*, 82.

Carn, S. A. (1999). Application of synthetic aperture radar (SAR) imagery to volcano mapping in the humid tropics: A case study in East Java, Indonesia. *Bulletin of Volcanology*, *61*(1-2), 92-105. doi: 10.1007/s004450050265

Di Traglia, F., Nolesini, T., Ciampalini, A., Solari, L., Frodella, W., Bellotti, F., ... Casagli, N. (2018). Tracking morphological changes and slope instability using spaceborne and ground-based SAR data. *Geomorphology*, *300*, 95-112. doi: 10.1016/j.geomorph.2017.10.023

Dietterich, H. R., Poland, M. P., Schmidt, D. A., Cashman, K. V., Sherrod, D. R., & Espinosa, A. T. (2012). Tracking lava flow emplacement on the east rift zone of Kīlauea, Hawai'i, with synthetic aperture radar coherence. *Geochemistry Geophysics Geosystems*, *13*(5), Q05001. doi: 10.1029/2011GC004016

Ebmeier, S. K., Andrews, B. J., Araya, M. C., Arnold, D. W., Biggs, J., Cooper, C., ... Williamson, J. L. (2018). Synthesis of global satellite observations of magmatic and volcanic deformation: implications for volcano monitoring & the lateral extent of magmatic domains. *Journal of Applied Volcanology*, *7*(1), 1-26. doi: 10.1186/s13617-018-0071-3

Escobar Wolf, R. and Ferres, D. (2018). Informe Tecnico: Volcan de Fuego. *Technical Report*, *Cooperacion Espanola*. Retrieved from `http://bibliotecadigital.aecid.es/bibliodig/i18n/consulta/registro.cmd?id=8751`

Fournier, T. J., Pritchard, M. E., & Riddick, S. N. (2010). Duration, magnitude, and frequency of subaerial volcano deformation events: New results from Latin America using InSAR and a global synthesis. *Geochemistry, Geophysics, Geosystems*, *11*(1). doi: 10.1029/2009GC002558

Global Volcanism Program. (2005). Report on Fuego (Guatemala) (Wunderman, R., ed.). *Bulletin of the Global Volcanism Network*, *30:8. Smithsonian Institution*. doi: 10 .5479/si.GVP.BGVN200508-342090

Goitom, B., Oppenheimer, C., Hammond, J. O., Grandin, R., Barnie, T., Donovan, A., ... Berhe, S. (2015). First recorded eruption of Nabro volcano, Eritrea, 2011. *Bulletin of Volcanology*, *77*(10), 85. doi: 10.1007/s00445-015-0966-3

ICC. (2021). *Instituto Privado de Investigación sobre Cambio Climático (ICC): El Platanar. [Online].* Retrieved Novemeber 2019, from `https://redmet.icc.org.gt/`

INSIVUMEH. (2018a). Descenso de flujos piroclasticos. *Bolentin Vulcanologico Especial*, *Volcan de Fuego*(36).

INSIVUMEH. (2018b). Erupcion con flujoc piroclasticos. *Bolentin Vulcanologico Especial*, *Volcan de Fuego*(27).

INSIVUMEH. (2018c). Finaliza la erupcion. *Bolentin Vulcanologico Especial*, *Volcan de Fuego*(33).

INSIVUMEH. (2018d). Flujos piroclasticos barranca las lajas y jute. *Bolentin Vulcanologico Especial*, *Volcan de Fuego*(38).

INSIVUMEH. (2018e). Lahares moderados en la barranca: Las lajas y honda. *Bolentin Vulcanologico Especial*, *Volcan de Fuego*(127).

Lei, T., Jia, X., Zhang, Y., He, L., Meng, H., & Nandi, A. K. (2018). Significantly fast and robust fuzzy c-means clustering algorithm based on morphological reconstruction and membership filtering. *IEEE Transactions on Fuzzy Systems*, *26*(5), 3027–3041.

Lopes, A., Nezry, E., Touzi, R., & Laur, H. (1993). Structure detection and statistical adaptive speckle filtering in SAR images. *International Journal of Remote Sensing*, *14*(9), 1735-1758. doi: 10.1080/01431169308953999

Lyons, J. J., Waite, G. P., Rose, W. I., & Chigna, G. (2010). Patterns in open vent, strombolian behavior at Fuego volcano, Guatemala, 2005-2007. *Bulletin of Volcanology*, *72*(1), 1-15. doi: 10.1007/s00445-009-0305-7

Martin, D. P., & Rose, W. I. (1981). Behavioral patterns of Fuego volcano, Guatemala. *Journal of Volcanology and Geothermal Research*, *10*(1-3), 67–81. doi: 10.1016/0377

-0273(81)90055-X

Meyer, F. J., McAlpin, D. B., Gong, W., Ajadi, O., Arko, S., Webley, P. W., & Dehn, J. (2015). Integrating SAR and derived products into operational volcano monitoring and decision support systems. *ISPRS Journal of Photogrammetry and Remote Sensing*, *100*, 106-117. doi: 10.1016/j.isprsjprs.2014.05.009

Moore, C., Wright, T., Hooper, A., & Biggs, J. (2019). The 2017 Eruption of Erta 'Ale Volcano, Ethiopia: Insights Into the Shallow Axial Plumbing System of an Incipient Mid-Ocean Ridge. *Geochemistry, Geophysics, Geosystems*, *20*(12), 5727-5743. doi: 10.1029/2019GC008692

Naismith, A. K., Armijos, M. T., Escobar, E. A. B., Chigna, W., & Watson, I. M. (2020). Fireside tales: understanding experiences of previous eruptions and factors influencing the decision to evacuate from activity of Volcán de Fuego. *Volcanica*, *3*(2), 205–226.

Naismith, A. K., Watson, I. M., Escobar-Wolf, R., Chigna, G., Thomas, H., Coppola, D., & Chun, C. (2019). Eruption frequency patterns through time for the current (1999–2018) activity cycle at Volcán de Fuego derived from remote sensing data: Evidence for an accelerating cycle of explosive paroxysms and potential implications of eruptive activity. *Journal of Volcanology and Geothermal Research*, *371*, 206–219.

Pallister, J. S., Schneider, D. J., Griswold, J. P., Keeler, R. H., Burton, W. C., Noyles, C., ... Ratdomopurbo, A. (2013). Merapi 2010 eruption-Chronology and extrusion rates monitored with satellite radar and used in eruption forecasting. *Journal of Volcanology and Geothermal Research*, *261*, 144-152. doi: 10.1016/j.jvolgeores.2012.07.012

Pardini, F., Queißer, M., Naismith, A., Watson, I., Clarisse, L., & Burton, M. (2019). Initial constraints on triggering mechanisms of the eruption of Fuego volcano (Guatemala) from 3 June 2018 using IASI satellite data. *Journal of Volcanology and Geothermal Research*, *376*, 54–61.

Patrick, M. R., Harris, A. J., Ripepe, M., Dehn, J., Rothery, D. A., & Calvari, S. (2007). Strombolian explosive styles and source conditions: Insights from thermal (FLIR) video. *Bulletin of Volcanology*, *69*(7), 769–784. doi: 10.1007/s00445-006-0107-0

Pritchard, M. E., Biggs, J., Wauthier, C., Sansosti, E., Arnold, D. W., Delgado, F., ... Zoffoli, S. (2018). Towards coordinated regional multi-satellite InSAR volcano observations: results from the Latin America pilot project. *Journal of Applied Volcanology*, *7*(1), 1-28. doi: 10.1186/s13617-018-0074-0

Small, D. (2011). Flattening gamma: Radiometric terrain correction for SAR imagery. *IEEE*

Transactions on Geoscience and Remote Sensing, *49*(8), 3081-3093. doi: 10.1109/TGRS.2011.2120616

Solikhin, A., Pinel, V., Vandemeulebrouck, J., Thouret, J. C., & Hendrasto, M. (2015). Mapping the 2010 Merapi pyroclastic deposits using dual-polarization Synthetic Aperture Radar (SAR) data. *Remote Sensing of Environment*, *158*, 180-192. doi: 10.1016/j.rse.2014.11.002

Wadge, G., Cole, P., Stinton, A., Komorowski, J. C., Stewart, R., Toombs, A. C., & Legendre, Y. (2011). Rapid topographic change measured by high-resolution satellite radar at Soufriere Hills Volcano, Montserrat, 2008-2010. *Journal of Volcanology and Geothermal Research*, *199*(1-2), 142-152. doi: 10.1016/j.jvolgeores.2010.10.011

Wadge, G., & Haynes, M. (1998). Cover Radar images growth of Soufriere Hills Volcano, Montserrat. *International Journal of Remote Sensing*, *19*(5), 797-800. doi: 10.1080/014311698215720

Wadge, G., Saunders, S., & Itikarai, I. (2012). Pulsatory andesite lava flow at Bagana Volcano. *Geochemistry, Geophysics, Geosystems*, *13*(11), 2012GC004336. doi: 10.1029/2012GC004336

Wadge, G., Scheuchl, B., & Stevens, N. F. (2002). Spaceborne radar measurements of the eruption of Soufrière Hills Volcano, Montserrat. *Geological Society Memoir*, *21*(1), 583-594. doi: 10.1144/GSL.MEM.2002.021.01.27

Werner, C., Wegmüller, U., Strozzi, T., & Wiesmann, A. (2000). Gamma SAR and interferometric processing software. In *Proceedings of the ers-envisat symposium, Gothenburg, Sweden* (Vol. 1620, p. 1620).